Ground-based observations of Saturn's auroral ionosphere over three days: trends in H_3^+ temperature, density and emission with Saturn local time and planetary period oscillation

James O'Donoghue [d,a], Henrik Melin [a], Tom S. Stallard [a], G. Provan [a], Luke Moore [d], Sarah V. Badman [e], Stan W.H. Cowley [a], Kevin H. Baines [c], Steve Miller [b], and James S.D. Blake [a]

[a] *Department of Physics and Astronomy, University of Leicester, Leicester, LE1 7RH, UK*

[b] *Atmospheric Physics Laboratory, Department of Physics and Astronomy, University College London, London, WC1E 6BT, UK*

[c] *NASA Jet Propulsion Laboratory, M/S 183-601, 4800 Oak Grove Drive, Pasadena, CA 91109, USA*

[d] *Center for Space Physics, Boston University, Boston, MA 02215, USA*

[e] *Department of Physics, Lancaster University, UK*

Key words: Saturn, aurora, magnetosphere, ionosphere, atmosphere

Abstract

On 19 to 21 April 2013, the ground-based 10-metre W.M. Keck II telescope was used to simultaneously measure H_3^+ emissions from four regions of Saturn's auroral ionosphere: 1) the northern noon region of the main auroral oval; 2) the northern midnight main oval; 3) the northern polar cap and 4) the southern noon main oval. The H_3^+ emission from these regions was captured in the form of high resolution spectral images as the planet rotated. The results herein contain twenty-three H_3^+ temperatures, column densities and total emissions located in the aforementioned regions - ninety-two data points in total, spread over timescales of both hours and days. Thermospheric temperatures in the spring-time northern main oval are found to be cooler than their autumn-time southern counterparts by tens of K, consistent with the hypothesis that the total thermospheric heating rate is inversely proportional to magnetic field strength. The main oval H_3^+ density and emission is lower at northern midnight than it is at noon, in agreement with a nearby peak in the electron influx in the post-dawn sector and a minimum flux at midnight. Finally, when arranging the northern main oval H_3^+ parameters as a function of the oscillation period seen in Saturn's magnetic field - the planetary period oscillation (PPO) phase - we see a large peak in H_3^+ density and emission at $\sim$115° northern phase, with a full-width at half-maximum (FWHM) of $\sim$44°. This seems to indicate that the influx of electrons associated with the PPO phase at 90° is responsible at least in part for the behavior of all H_3^+ parameters. A combination of the H_3^+ production and loss timescales and the $\pm$10° uncertainty in the location of a given PPO phase are likely, at least in part, to be responsible for the observed peaks in H_3^+ density and emission occurring at a later time than the peak precipitation expected at 90° PPO phase.

1 Introduction

1.1 Ionosphere

Saturn's ionosphere is thought to be dominated by the positive ions H^+ and H_3^+ between 900 - 3000 km altitude and by hydrocarbon ions (e.g. $C_3H_5^+$) between 500 - 900 km altitude, along with their companion electrons, which maintain the ionosphere's quasi-neutrality (*Moses and Bass*, 2000). Co-located with this is the thermosphere, the charge-neutral component of the upper atmosphere, which is composed chiefly of H and H_2. Charged particles in the ionosphere are continuously generated by ionising the otherwise neutral thermosphere through two main mechanisms. The first, photo-ionisation by solar extreme ultra-violet (EUV) radiation, acts across the entire sunlit portion of the planet (the dayside). The second, electron impact ionisation, acts primarily in the polar regions of the planet. Both mechanisms also electronically, vibrationally and rotationally excite the atmospheric constituents, which in turn de-excite and emit photons. The emissions from these mechanisms are 'auroral' emissions and occur at multiple wavelengths including infrared (IR), visible and ultraviolet (UV). This paper focuses primarily on the infrared emissions emanating from the molecular ion H_3^+ near the poles of the planet.

Saturn's ionosphere lies at the base of the planetary magnetosphere, a region formed by the confinement of the planetary magnetic field by the solar wind. Closed field lines extend in the equatorial region to distances $\sim$22 R_S (R_S is Saturn's 1 bar equatorial radius, equal to 60,268 km) on the dayside (*Radioti et al.*, 2013), while open field lines stretch into a long magnetic tail downstream from the planet on the nightside. From estimates of the open flux in the magnetotail, the boundary between open and closed field lines in the ionosphere typically lies at around planetocentric co-latitude $\sim$15° in each hemisphere (*Badman et al.*, 2006), the difference between the two reflecting the north-south quadrupole asymmetry of Saturn's planetary magnetic field (*Burton et al.*, 2010). In general it is expected that field-aligned currents flow down into the ionosphere over the polar field region due to the sub-corotation of plasma on open field lines and in the outer magnetosphere (*Bunce et al.*, 2008). The current then flows from the pole towards the equator in both hemispheres as ionospheric Pedersen currents, before returning up the field lines to the magnetosphere at lower latitudes as the flow returns to near-rigid corotation with the planet (e.g. *Cowley and Bunce*, 2003; *Cowley et al.*, 2004). The main auroral oval emissions are related to the latter ring of upward current (downward electron precipitation). The auroral oval is thus expected to lie in the region just equatorward of the open-closed boundary where the plasma angular velocity rises from low values on open lines towards rigid corotation on closed lines. The main oval is in general taken to correspond to the region between co-latitudes of $\sim 10°$ and $\sim 20°$ in both hemispheres (see, e.g., *Carbary*, 2012, and references therein). Auroral emissions are also sometimes observed in the poleward region, likely associated with solar wind-magnetosphere coupling dynamics at the magnetopause boundary of the magnetosphere (e.g. *Meredith et al.*, 2014). Here we present new observations of H_3^+ obtained with the Keck telescope in April 2013 using similar methodology to that employed by *O'Donoghue et al.* (2014). These observations measure the northern and southern main auroral ovals simultaneously as in the previous study, but this time they take place over three days instead of one, allowing for a wider ranging analysis of short term auroral behavior. In addition, due to the developing northern spring season at Saturn, the dataset presented here also includes and discusses simultaneous measurements of both the northern polar aurora as well as the midnight main auroral oval, owing to the viewing geometry at the time of the observations.

1.2 The H_3^+ probe at Saturn

The molecular ion H_3^+ is produced by the reaction $H_2 + H_2^+ \longrightarrow H_3^+ + H$ (*Oka*, 2006). The reaction time (the ion chemistry timescale) varies from 10 seconds at 800 km altitude to 1000 seconds for altitudes near 2000 km (*Badman et al.*, 2014). The lifetime of H_3^+ is proportional to its temperature, inversely proportional to the ionospheric electron density and has been previously quoted as 500 seconds (*Melin et al.*, 2011). During this lifetime, H_3^+ becomes thermally excited to a higher rotational-vibrational (ro-vibrational) state by neighboring molecules on timescales of 10^{-2} s, which is approximately the same time for the ion to relax to a lower state and emit a photon. The discrete emission line spectra of H_3^+ make it a useful probe of the conditions in Saturn's ionosphere for two reasons. The first is that H_3^+ parameters such as column-integrated temperature, density and power output (hereafter, total emission) can be derived from it (e.g. *Miller et al.*, 2006; *Melin et al.*, 2014). Secondly, it is considered to be in local thermodynamic equilibrium (LTE) - or at least quasi-LTE - with its surroundings (*Miller et al.*, 1990; *Moore et al.*, 2008), meaning that the ion temperature is equivalent to the neutral temperature.

Using the ground-based 3.8-metre United Kingdom InfraRed Telescope (UKIRT), the southern auroral H_3^+ temperature was found to be 380 $\pm$70 K in 1999 and 420 $\pm$70 K in 2004 by *Melin et al.* (2007). Later, in 2007, the Visual and Infrared Mapping Spectrometer (VIMS) (*Brown et al.*, 2004) on board Cassini was used to derive a southern polar auroral H_3^+ temperature of (on average) 590 $\pm$30 K over a period of 10 hours (*Stallard et al.*, 2012a). Measurements of the southern auroral oval at equinox in 2009, also obtained by Cassini VIMS, yielded average temperatures of $\sim$410 K (*Lamy et al.*, 2013). The first conjugate northern and southern main oval H_3^+ temperatures were measured at high spatial resolution in 2011 using the 10-metre W.M. Keck II (hereafter, Keck) telescope by *O'Donoghue et al.* (2014). The 10 spectral images, when co-added, yielded an average main auroral H_3^+ temperature of 583 $\pm$13 K (south) and 527 $\pm$18 K (north) over a $\sim$2 hour period. Throughout this time interval the spectra gave temperatures that varied by tens of Kelvins; this was a similar variability to the uncertainties, so it may be considered real or due to noise. In the neutral thermosphere near the exobase ($\sim$1900 km altitude above the 1 bar surface), solar occultations were performed using the Cassini ultraviolet imaging spectrometer (UVIS) to derive temperatures (*Koskinen et al.*, 2013), yielding temperatures of 370 K to 540 K from low- to high(auroral)-latitudes, respectively. The inter-hemispheric temperature asymmetry measured by *O'Donoghue et al.* (2014) was postulated to be the result of an inversely proportional relationship between magnetic field strength and the total heating rate. Due to the lower magnetic field strength in the south, the area undergoing heating is larger in the south than in the north (see *O'Donoghue et al.*, 2014, for a more detailed discussion). Whilst the thermospheric temperatures at high latitudes can mostly be explained via auroral region Joule heating (*Cowley et al.*, 2004), the low-latitude high temperatures remain difficult to explain theoretically. For example, exospheric temperatures are modeled to be 143 Kelvin on the basis of solar EUV heating alone, yet observations show the exosphere to be ∼400 K (at sub-auroral latitudes) (*Yelle and Miller*, 2004; *Koskinen et al.*, 2013). *Smith et al.* (2007) and *Mueller-Wodarg et al.* (2012) have explored the idea that heat is meridionally transported down from the poles to the equator, but conclude that auroral heating actually provides a net cooling effect at low latitudes. This is caused by a circulation pattern in which high altitude heating (by ion drag) causes equatorward flows. The flow is balanced by the continuity equation at low altitudes in the form of poleward flows, which themselves require there be an upwelling of material from below. It is this upwelling material that expands and cools adiabatically, leading to the counter intuitive effect of low latitude cooling, despite there being a nearby heating source (*Smith et al.*, 2007). Thus, at present, it appears some additional source of energy is required to explain equatorial temperatures. One suggestion is the breaking of gravity waves in the thermosphere, but this is modeled to account for temperature enhancements of (at most) ∼10's of K (*Barrow and Matcheva*, 2013). A final source of note is the low-latitude precipitation along the magnetic field lines conjugate to the rings known as 'ring rain'; it is possible that this is also associated with a low-latitude current system between the rings and the planet, but as yet such currents have not been directly observed (*O'Donoghue et al.*, 2013).

1.3 Planetary period oscillations

In 1980 both Voyager 1 and 2 spacecraft measured bursts of nonthermal radio emission which emanated from Saturn - specifically they are likely from the northern hemisphere: the period of these bursts were ~10.67 hours and taken (provisionally) to be the intrinsic rotation period of the planet (*Kaiser et al.*, 1980). However, more recently, during Saturn's pre-equinoctial southern summer between 2004 - 2008, the Cassini spacecraft has measured Saturn kilometric radiation (SKR) from both the northern and southern hemispheres, finding them to exhibit different periods: ~10.6 hours in the north and ~10.8 hours in the south (although these rates are still changing over time) (*Gurnett et al.*, 2009). These emissions, together with magnetic field perturbations observed within the magnetosphere, are inferred to be associated with two independent current systems rotating in the northern and southern hemispheres with slightly differing periods that vary slowly with Saturn's seasons (see, e.g. *Andrews et al.*, 2008, 2010; *Southwood*, 2011; *Provan et al.*, 2009, 2012, and references therein). Following the recent discussion by *Southwood and Cowley* (2014), the empirically-determined current system associated with the northern ionosphere, of primary interest here, is shown in Figure 1, in a view looking down on the northern pole (a similar current system also flows in the south) (*Hunt et al.*, 2014). In this diagram the solid lines and symbols show the currents, while the dotted lines represent the associated magnetic field perturbations above the Pedersen layer of the ionosphere required by Ampère's law. The primary current system consists of field-aligned currents that flow down into the ionosphere on the right of the diagram (circled crosses on the inner dashed line ring), across the polar ionosphere as Pedersen currents directed from right to left, and out of the ionosphere as field-aligned currents on the left of the diagram (circled dots on the black dashed line ring). Secondary field-aligned currents of lesser magnitude and opposite polarity also flow on the outer ring, which serve to limit the field perturbations to the interior region. This current system then rotates with the northern period, ~10.64 h at the time of our observations (compared with ~10.69 h for the southern SKR period). Position with respect to the rotating pattern is defined by the northern PPO phase function Ψ_N, which increases clockwise around the diagram in Figure 1. Enhanced upward currents, associated with enhanced electron precipitation and auroral emissions, are expected to occur for $\Psi_N \approx 90°$ (modulo 360°), while enhanced downward currents, likely associated with suppression of precipitation and emissions, are expected for $\Psi_N \approx 270°$.

Empirically, the orientation of the system at any time is determined through examination of the related magnetic field oscillations. In particular, if we consider the magnetic perturbations between the two current rings (dotted lines in Figure 1), mapped along quasi-dipolar field lines into the equatorial magnetosphere, it will be seen that these transform into a quasi-uniform field in which the perturbation field points radially outward from the planet at $\Psi_N \approx 0°$, radially inward at $\Psi_N \approx 180°$, and has positive and negative azimuthal components (with respect to the northern spin/magnetic pole) at $\Psi_N \approx 90°$ and 270°, respectively. Magnetic oscillations observed in the equatorial magnetosphere are then analysed to determine the azimuth with respect to noon at which the northern quasi-uniform perturbation field points radially outward at any instant of time, $\Phi_N(t)$, thus also defining the azimuth where the northern PPO phase Ψ_N takes the value zero (modulo 360°) at that time. The northern PPO phase as a function of azimuth and time is thus given by

$$\Psi_N(\phi, t) = \Phi_N(t) - \phi, \qquad (1)$$

where ϕ is the azimuth in degrees with respect to noon of any observation point (equivalent to local time), and $\Phi_N(t)$ is determined empirically, with rotation period given by $\tau_N = 360°/(\mathrm{d}\Phi_N/\mathrm{d}t)$ and with Φ_N expressed in degrees. The function $\Phi_N(t)$ employed here is that determined from Cassini magnetic field data by *Provan et al.* (2014). Signatures of this planetary period oscillation from the auroral region were first noted from the Voyager 1 and 2 spacecraft's UV photometer data by *Sandel and Broadfoot* [1981] and *Sandel et al.* [1982].

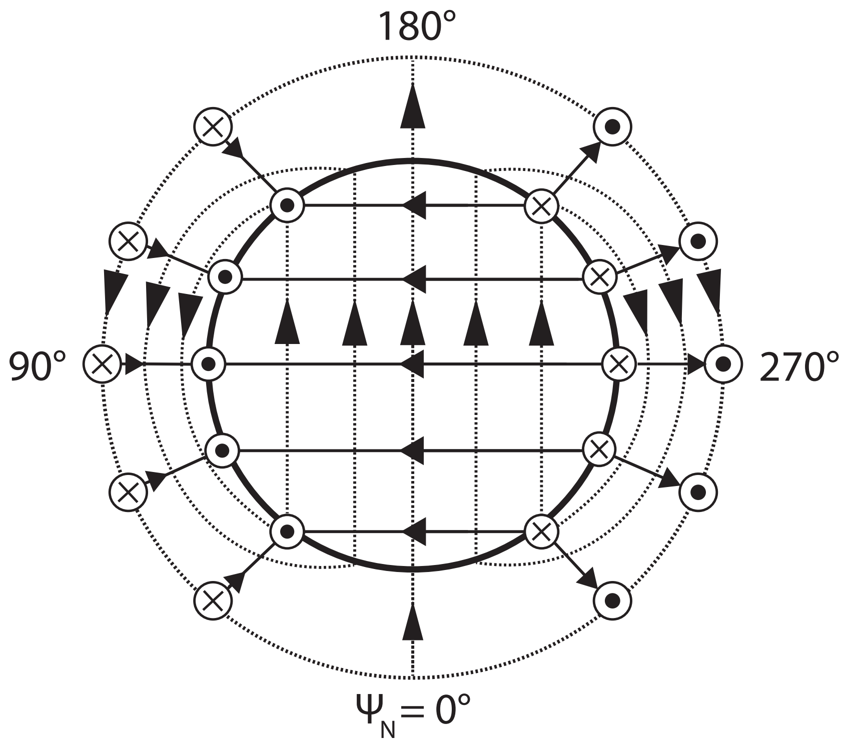

Fig. 1. Sketch of the form of the currents (solid lines and symbols) and perturbation magnetic fields (dotted lines) associated with the northern system PPOs, in a view looking down on Saturn's northern ionosphere from above. The principal field-aligned currents flow across the inner ring: into the ionosphere on the right (circled crosses), and out of the ionosphere on the left (circled dots), joined by ionospheric Pedersen currents flowing from right to left across the polar ionosphere. Secondary field-aligned currents of smaller magnitude and opposite polarity flow on the outer boundary of the current system, confining the perturbation field to the interior region. The current system rotates anti-clockwise with the northern PPO period τ_N. Azimuth with respect to the current system is defined by the phase function $\Psi_N(\phi, t)$ as shown in the figure (equation (1)), increasing clockwise around the diagram.

Using Cassini VIMS, *Badman et al.* [2012a] discovered that the H_3^+ auroral intensity follows a sinusoidal function with PPO phase, with H_3^+ peak intensity occurring in the north between $\Psi_N \approx 0$ - 45°, before the expected maximum peak intensity associated with enhanced electron precipitation at $\Psi_N \approx 90^\circ$.

2 Observations

The observations presented here used the 10-m Keck telescope situated on Mauna Kea, Hawaii. They were designed to be an integral part of the Saturn Auroral Observing Campaign of 2013 (this Icarus special issue), such that they overlap observations performed by the Cassini spacecraft, Hubble Space Telescope, and the NASA Infrared Telescope Facility (IRTF). The observations took place on the 19, 20, and 21 April and are summarized in Table 1. In this table the quoted times are the actual observing time on Earth (i.e. not corrected for light-travel time from Saturn to Earth) and the 'seeing' column refers to blurring of the received light by the Earth's atmosphere. The quoted central meridian longitudes (CMLs) are from the Saturn system III longitude system [*Kaiser et al.* 1980]. Emissions from these CMLs are light travel time corrected, i.e. the ∼73 minutes time delay has been accounted for in the results here. During these dates, Saturn was at opposition with respect to the Earth-Sun line with its northern hemisphere tilted towards the Earth and the Sun with both a sub-Earth and sub-solar latitude (coincidently) of 18.3°, i.e. in conditions of Saturn's northern spring (summer solstice occurs in 2017). In the previous work, Saturn had a sub-Earth latitude of 8.2° [*O'Donoghue et al.* 2014].

Date	Start UT	End UT	Saturn integration*	CML range	Seeing
19 April	10:55:00	13:11:50	40 min (8)*	43 - 120°	0.4″
20 April	12:18:42	13:18:39	20 min (4)*	181 - 215°	0.45″
21 April	10:40:05	13:24:41	55 min (11)*	217 - 309°	0.6″

Table 1

Summary of Keck telescope observations in April 2013. *Total time spent observing Saturn itself; the number in parentheses is the number of 5-minute co-additions used.

The instrument used on the Keck telescope was the near infrared spectrometer (NIRSPEC) [*McLean et al.* 1998], which has a spectral resolving power of R = $\lambda/\Delta\lambda$ ∼25,000 and thus provides a minimum resolution of (e.g.) $\Delta\lambda \approx 1.59$ x 10^{-4} μm at 3.975 μm. The wavelength range used here is between 3.95 and 4.0 μm, which covers the Q-Branch (ΔJ=0) ro-vibrational transition lines of H_3^+. Saturn's axis of rotation is measured to be co-aligned with the magnetic axis to within ~0.1° uncertainty [*Burton et al.* 2010]. Taking advantage of this symmetry, the spectrometer slit was orientated in a north-south direction on Saturn as shown in Figure 2. The planet is then allowed to rotate beneath the slit whilst spectral images are taken along the noon-midnight meridian plane. The slit measures 0.432″ width by 24″ length with a pixel on the CCD corresponding to 0.144″ squared on the sky, as in Figure 2.

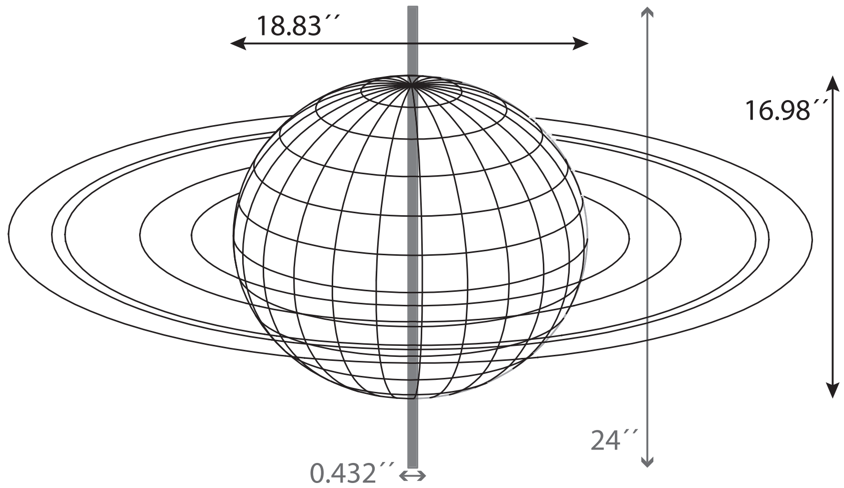

Fig. 2. **Saturn as observed with Keck, April 21 2013.** Saturn's sub-Earth latitude was 18.3° during the observations. The arrowed lines show the angular extent of Saturn and the dimensions of the NIRSPEC spectral slit in seconds of arc.

Owing to this viewing geometry we are afforded the ability to collect data from four distinct latitudinal ranges:

(1) Northern midnight main oval (NMMO): 8 - 15° co-latitude (Nightside)
(2) Northern polar cap (NPC): 0 - 6° co-latitude (Day - Nightside)
(3) Northern main oval (NMO): 8 - 22° co-latitude (Dayside)
(4) Southern main oval (SMO): 18 - 22° co-latitude (Dayside)

where dayside and nightside correspond to regions sunward and anti-sunward of the kronographic north pole, respectively. These regions of interest are shown in Figure 3 and note that they all remain lit by the Sun. They were selected (as close as the viewing geometry allowed) to coincide with the approximate statistical locations of the northern and southern main auroral ovals between ∼10 - 25°, and the polar cap between ±10° of the north pole [*Badman et al.* 2006; *Carbary* 2012]. These regions are associated with internal and external forcing on the Saturnian magnetosphere, respectively, as discussed in the introduction. An example of the viewing geometry limitation is at the NPC - here, the spatial resolution of one pixel on the detector corresponds to ∼3° latitude. In addition, and applicable to the whole spectral image, atmospheric seeing will smear the signal received across multiple pixels. Although the amount of pixels smeared is constant within the image, the range of latitudes represented by a given pixel diminishes with increasing latitude. This cross-contamination by light from neighbouring pixels is taken into account by creating a small separation of between ∼0.144 - 0.288 seconds of arc (1 - 2 pixels) between the different regions listed above.

Each individual spectral image consists of twelve 5-s integrations, creating exposures 60 s long, which are of both Saturn 'A' and sky 'B' frames, with the telescope slewing between each in the sky in an ABBA pattern. Standard astronomical reduction techniques are employed to clean the observed spectral images, which include an A-minus-B subtraction in which the Earth's sky emissions are removed from the Saturn spectra, and a star flux calibration. The flux calibration measures the spectrum of a black body emitting star (A0) in order to account for the wavelength dependent absorption of light by the Earth's atmosphere, whilst also converting the CCD photon count into physical photon flux. The star used in this work was HR 5717. Other reduction procedures include a dark current subtraction and dividing by a 'flat field'. Together, these account for thermal emissions at the detector and defects on the CCD chip and optics, respectively. The reduced spectral images are then co-added into groups of five spectra (see Table 1) in order to create a single higher signal to noise (S/N) ratio image. However,

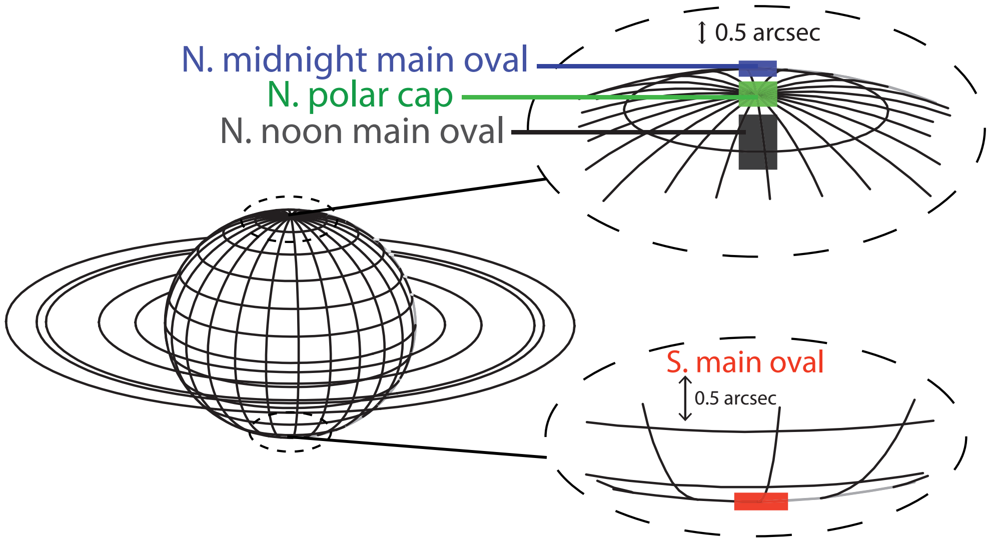

Fig. 3. **Regions of interest on Saturn.** Four distinct color-coded areas are illustrated, corresponding to the regions listed in the text. The chosen color scheme will be used in subsequent figures for clarity. Note that the different colored blocks (not to exact scale) are separated slightly in the north, to avoid cross-contamination introduced by the effects of telluric seeing. Longitude and latitude grid lines represent 15 degree spacings.

these spectra are obtained at different times typically within a ~15 - 20 minute range; this is chiefly because the A frames are often separated by B frames, but more general observing time overheads cause this time window to vary, e.g. the telescope slewing time between the A and B frame positions, losses in tracking or human error. Within these time ranges we thus typically obtain a swath of data spanning 8 - 11 ° in longitude as the planet rotates beneath the slit. In this work we assume an optically thin atmosphere in and above the ionosphere; this assumption was used and tested by *Lam et al.* [1997] to be valid.

An example of a reduced spectral image (x-axis wavelength, y-axis spatial dimension) which has been co-added from all 5-minute integrations on April 21 is shown in Figure 4. In this figure there are three main sources of radiation highlighted: the reflection of sunlight from the lower atmosphere, the continuum reflection of sunlight from the rings, and discrete H_3^+ emission lines. The ability to measure H_3^+ emissions is aided by the fact that hydrocarbons also absorb sunlight at different wavelengths; these are the dark regions on the body of the planet between 5 and 19 arcseconds in Figure 4.

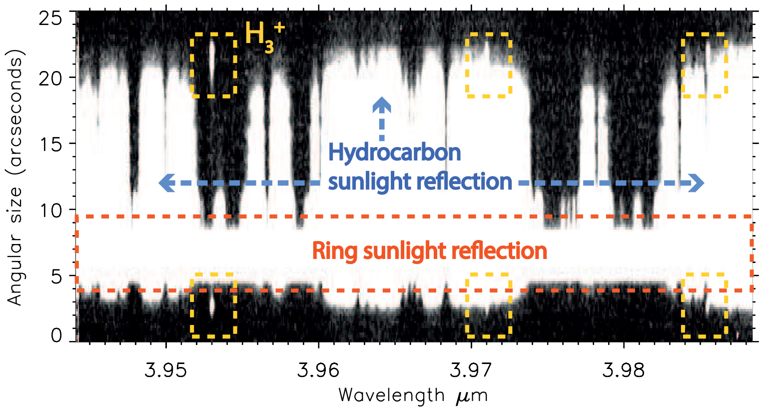

Fig. 4. **An image of the spectrum of Saturn taken at local Saturn noon.** This is the co-addition of all eleven 5-minute integrations on 21 April 2013. The wavelength range is shown on the horizontal axis and the angular size in the sky is shown on the vertical axis. North is at the top of the image and south is at the bottom. Discrete H_3^+ emission line spectra are inside the yellow dashed boxes in the form of white vertical lines (white being high light intensity, black being low/none). From left to right these lines are the $Q(1,0^-)$, $Q(2,1)$ and $Q(3,0)$ lines described in the main text. Hydrocarbons such as methane absorb solar radiation (creating the black background) between the auroral regions. The white bar of emission centered at $\sim 6''$ is the continuum reflection of sunlight from the rings. The remaining white pixels are due to sunlight reflected by hydrocarbons and other molecules.

3 Data analysis

For a given temperature, a discrete H_3^+ emission line will emit at a given intensity. We produce a theoretical spectrum of multiple lines from a line list of H_3^+ emission for thousands of different temperatures [see e.g. *Neale et al.* 1996; *Melin et al.* 2014]. The relative intensities of multiple discrete H_3^+ emission lines (i.e. a set of line ratios) represent the effective temperature of H_3^+ in quasi-LTE. An example of an observed spectral profile is shown in Figure 5 by the black crosses. Three Q-branch ($\Delta J = 0$) intensity peaks are visible from left to right in this

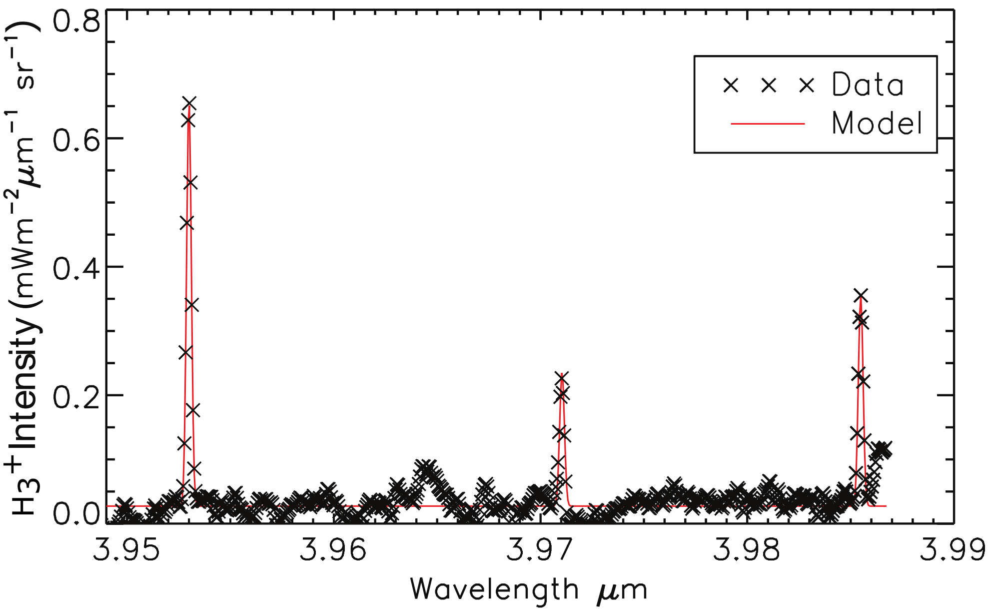

Fig. 5. **Model fit to H_3^+ intensity as a function of wavelength.** This spectral profile is produced from the co-add of all northern main oval images on April 21 (NMO; 8 - 22° co-latitude). The x- and y-axes show wavelength and intensity of H_3^+ emission, respectively. The latter is indicated by the black crosses for the observed emission and the model fit to the spectrum is shown in red. The temperature derived for this spectral profile is 404 ± 11 K.

figure; Q(1,0$^-$), Q(2,1) and Q(3,0). These have transition energies ω between upper (j) and lower (i) ro-vibrational energy states of $\omega_{i,j} = 2529.721$ cm^{-1}, $\omega_{i,j} = 2514.619$ cm^{-1} and $\omega_{i,j} = 2509.074$ cm^{-1}, respectively (further transition line information is available in Table 1 of *Kao et al.* [1991]). The modeled theoretical spectrum is reproduced for a variety of temperatures until a close match is found to the observed spectrum by least-squares fitting. In other words, the effective column-integrated temperature of H_3^+ is found by comparing the observed line ratios to model values.

Emission by H_3^+ depends upon its temperature with, in general, a higher temperature leading to a spectral transition line of higher intensity. The emission we observe at the detector (following the data reduction) is representative of a line-of-sight column-integrated quantity of molecules: the column density. Thus by dividing the observed intensity by the intensity of a single molecule we can determine the number of molecules in the column, in units of molecules per square metre (m^{-2}).

The effective total emission of H_3^+ is the result of the multiplication of the integrated emission per molecule across all wavelengths by the column density, giving a measurement of the total emitted power by H_3^+ as follows [*Lam et al.* 1997]:

$$E(H_3^+) = E_{mol}(H_3^+, T) \times N(H_3^+, T) \ , \tag{2}$$

where $E_{mol}(H_3^+, T)$ is the integrated intensity of a H_3^+ line between 0.75 - 22 microns

$$E_{mol}(H_3^+) = a + bT + cT^2 + dT^3 + eT^4 \ . \tag{3}$$

modeled for a particular temperature, T. Parameters a to e are partition function constants detailed and given by *Miller et al.* [2010]. As such, it is a direct measure for the rate of cooling of the ionosphere/thermosphere by H_3^+, which is itself responsible for some of the cooling in the thermosphere [*Grodent et al.* 2001; *Raynaud et al.* 2004; *Miller et al.* 2010].

The line-of-sight column density attains a useful physical meaning if it is corrected to the altitude of a column that extends vertically from Saturn's surface. Thus each such measurement needs to be reduced by some factor dependent upon the angle to the local vertical of the observation. Observations by the Cassini spacecraft show that the majority of the H_3^+ intensity is located within the 800 - 1400 km range of altitudes above the 1 bar pressure surface [*Stallard et al.* 2012b]. Models are in agreement with this, predicting that the majority of ionospheric H_3^+ ions (approximately >90% by number density) are located in this same 600 km range of altitudes [e.g. *Mueller-Wodarg et al.* 2012]. By considering two oblate spheroids (with elliptical cross-sections) of Saturn tilted at 18.3° relative to the observer, the inner spheroid being the 1-bar pressure surface of Saturn plus 800 km, and the outer spheroid being at plus 1400 km altitude of the same surface, we calculated the depth of the column we observe as a function of latitude. The observed line of sight column of atmosphere becomes larger nearer the poles, compared to at the equator, and this is corrected for by reducing the measured intensity as a function of latitude to a normalised value.

The spectrum of H_3^+ can be described as a 'spectral function': this function is a sum of Gaussian fits to all of the ro-vibrational transition lines and depends on the temperature and density of H_3^+. The temperature and density uncertainties from this are found by applying Cramer's rule, whilst the uncertainty in total emission is found by using basic error propagation formulae [see *Melin* 2006; *Melin et al.* 2014, and references therein]. As the temperature and density parameters are found using a least-squares fit embedded within the H_3^+ fitting routine, they are an indicator of the quality of the spectral fit.

The most optimal (lowest) seeing achieved herein is $0.4''$, which amounts to 2560 km perpendicular to the line-of-sight at a distance of 8.826 astronomical units (the Earth-Saturn distance on April 20). Therefore, even in the extreme case of a measurement of H_3^+ on or near the Saturnian limb, we are still capturing the entire column of altitude in which H_3^+ is distributed above the 1-bar surface. This means that variability in H_3^+ parameters that we report herein should be considered due to variations in latitude and longitude and not in altitude which is column-integrated at any location.

4 Results and discussion

The total time spent observing in this campaign, including sky exposures of the sky, calibrations and general time-overheads (e.g. moving the telescope), was 361 minutes. The total integration time on Saturn itself was 115 minutes. The exposure times and values of temperature, column density, and total emission for the northern and southern main ovals (NMO and SMO) and northern polar cap and midnight oval (NPC and NMMO) are shown in Tables 2, 3 and 4 for April 19, 20 and 21, respectively. The start and end universal times (UT) in the tables correspond to the start of the first Saturn exposure (A frame) and the end of the final (fifth) A frame; as mentioned earlier, observing time overheads do not permit a continuous 5-minute acquisition.

Average parameters for each day are shown in two different ways in this section. The first is the average of all individually model-fitted spectra for a given parameter over a given observation night; these are represented by the dashed horizontal lines in each of the figures (6 - 9 inclusive). Note that the values in the first row of Table 2 have unusually high uncertainties, perhaps due to passing cirrus clouds during the observations; as such, they are not used when calculating the averages. A second type of averaging, the 'co-average', is found by fitting a model H_3^+ spectrum to the co-addition of all spectral images from each region for each day. This ensures that the maximum possible S/N is obtained prior to fitting itself. These co-added averages have higher S/N and lower uncertainty than an individually fitted spectral image and are given in Tables 2, 3 and 4, although the difference between the two types of averaging are small.

Start (UT)	End (UT)	T_{NMO} (K)	T_{NPC} (K)	T_{NMMO} (K)	T_{SMO} (K)	CD_{NMO} (10^{15} m^{-2})	CD_{NPC} (10^{15} m^{-2})	CD_{NMMO} (10^{15} m^{-2})	CD_{SMO} (10^{15} m^{-2})	E_{NMO} ($10^{-5}Wm^{-2}sr^{-1}$)	E_{NPC} ($10^{-5}Wm^{-2}sr^{-1}$)	E_{NMMO} ($10^{-5}Wm^{-2}sr^{-1}$)	E_{SMO} ($10^{-5}Wm^{-2}sr^{-1}$)
10:55	11:18	994 ± 900	925 ± 587	699 ± 212	453 ± 67	0.04 ± 0.06	0.03 ± 0.05	0.03 ± 0.05	0.5 ± 0.5	0.70 ± 0.09	0.37 ± 0.09	0.12 ± 0.02	0.11 ± 0.07
11:23	11:50	389 ± 34	356 ± 32	501 ± 48	466 ± 39	7.4 ± 5.3	10.2 ± 8.6	0.3 ± 0.2	0.7 ± 0.4	0.40 ± 0.37	0.23 ± 0.46	0.14 ± 0.02	0.18 ± 0.03
11:51	12:05	449 ± 38	394 ± 37	506 ± 58	361 ± 30	2.5 ± 1.5	4.1 ± 3.2	0.3 ± 0.2	6.3 ± 4.9	0.46 ± 0.14	0.25 ± 0.21	0.12 ± 0.02	0.17 ± 0.20
12:09	12:22	376 ± 32	496 ± 41	438 ± 50	583 ± 54	10.3 ± 7.8	1.0 ± 0.5	0.7 ± 0.6	0.2 ± 0.1	0.41 ± 0.47	0.39 ± 0.05	0.11 ± 0.05	0.24 ± 0.01
12:23	12:36	396 ± 26	428 ± 32	435 ± 38	498 ± 46	9.0 ± 4.9	2.8 ± 1.6	0.9 ± 0.6	0.5 ± 0.3	0.56 ± 0.25	0.34 ± 0.10	0.13 ± 0.04	0.20 ± 0.03
12:41	12:53	417 ± 32	372 ± 32	471 ± 54	398 ± 51	5.2 ± 3.2	7.8 ± 6.0	0.6 ± 0.5	1.9 ± 2.1	0.52 ± 0.21	0.27 ± 0.31	0.16 ± 0.04	0.13 ± 0.14
12:54	13:07	382 ± 49	451 ± 33	395 ± 34	479 ± 45	11.4 ± 11.4	2.0 ± 1.0	2.1 ± 1.5	0.6 ± 0.4	0.52 ± 0.62	0.38 ± 0.07	0.13 ± 0.08	0.18 ± 0.03
13:11	13:24	407 ± 22	467 ± 38	436 ± 45	444 ± 41	7.9 ± 3.5	1.4 ± 0.8	0.7 ± 0.6	1.0 ± 0.7	0.64 ± 0.17	0.37 ± 0.06	0.10 ± 0.05	0.17 ± 0.05
Co-average*:	402 ± 20	441 ± 16	466 ± 20	442 ± 23	6.4 ± 2.5	2.0 ± 0.5	0.5 ± 0.1	0.9 ± 0.4	0.47 ± 0.02	0.31 ± 0.04	0.12 ± 0.02	0.15 ± 0.03	0.15 ± 0.03
Mean value	404 ± 13	423 ± 13	455 ± 18	460 ± 17	7.7 ± 2.3	4.2 ± 1.6	0.8 ± 0.3	1.5 ± 0.7	0.50 ± 0.12	0.32 ± 0.09	0.13 ± 0.02	0.17 ± 0.03	0.17 ± 0.03

Table 2

Saturn's auroral/polar properties as a function of time on 19 April 2013. All uncertainties shown are one standard deviation (i.e. 1-sigma errors). T, CD and E are temperature, column density and total emission of H_3^+, respectively. *Co-averages are co-add averages formed from applying a model fit to the co-addition of all spectra from the night, rather than of the individual values, whilst the mean values are drawn from the table. Note that the first row is not used in the latter average due to very high uncertainties.

Start (UT)	End (UT)	T_{NMO} (K)	T_{NPC} (K)	T_{NMMO} (K)	T_{SMO} (K)	CD_{NMO} (10^{15} m^{-2})	CD_{NPC} (10^{15} m^{-2})	CD_{NMMO} (10^{15} m^{-2})	CD_{SMO} (10^{15} m^{-2})	E_{NMO} ($10^{-5}Wm^{-2}sr^{-1}$)	E_{NPC} ($10^{-5}Wm^{-2}sr^{-1}$)	E_{NMMO} ($10^{-5}Wm^{-2}sr^{-1}$)	E_{SMO} ($10^{-5}Wm^{-2}sr^{-1}$)
12:18	12:31	461 ± 42	426 ± 35	476 ± 33	475 ± 41	2.3 ± 1.5	2.5 ± 1.6	0.7 ± 0.3	0.7 ± 0.4	0.54 ± 0.13	0.31 ± 0.11	0.2 ± 0.03	0.21 ± 0.03
12:31	12:46	476 ± 37	423 ± 33	459 ± 32	460 ± 32	2.1 ± 1.1	2.8 ± 1.7	0.7 ± 0.4	1.1 ± 0.5	0.61 ± 0.09	0.32 ± 0.11	0.15 ± 0.03	0.24 ± 0.03
12:51	13:03	442 ± 34	377 ± 27	439 ± 31	496 ± 35	3.3 ± 1.9	7.1 ± 4.4	1.0 ± 0.5	0.6 ± 0.3	0.53 ± 0.14	0.29 ± 0.23	0.15 ± 0.03	0.23 ± 0.02
13:07	13:18	441 ± 31	503 ± 37	562 ± 47	441 ± 39	3.1 ± 1.6	0.8 ± 0.4	0.2 ± 0.1	1.2 ± 0.8	0.49 ± 0.13	0.34 ± 0.04	0.19 ± 0.01	0.19 ± 0.05
Co-average*	441 ± 22	423 ± 15	471 ± 17	454 ± 22	3.3 ± 1.3	2.8 ± 0.7	0.6 ± 0.2	1.0 ± 0.4	0.54 ± 0.09	0.31 ± 0.05	0.17 ± 0.01	0.22 ± 0.02	0.22 ± 0.02
Mean value	453 ± 20	434 ± 20	487 ± 22	468 ± 19	2.8 ± 0.9	3.6 ± 1.6	0.6 ± 0.3	0.9 ± 0.3	0.54 ± 0.07	0.31 ± 0.09	0.16 ± 0.02	0.22 ± 0.02	0.22 ± 0.02

Table 3

As Table 2, but for data obtained on 20 April 2013.

Start (UT)	End (UT)	T_{NMO} (K)	T_{NPC} (K)	T_{NMMO} (K)	T_{SMO} (K)	CD_{NMO} (10^{15} m^{-2})	CD_{NPC} (10^{15} m^{-2})	CD_{NMMO} (10^{15} m^{-2})	CD_{SMO} (10^{15} m^{-2})	E_{NMO} (10^{-5}Wm^{-2}sr^{-1})	E_{NPC} (10^{-5}Wm^{-2}sr^{-1})	E_{NMMO} (10^{-5}Wm^{-2}sr^{-1})	E_{SMO} (10^{-5}Wm^{-2}sr^{-1})
10:40	10:53	375 ± 18	397 ± 25	525 ± 40	375 ± 30	23.9 ± 10.0	9.6 ± 5.0	0.4 ± 0.2	4.5 ± 3.2	0.89 ± 0.27	0.61 ± 0.14	0.23 ± 0.01	0.17 ± 0.14
10:54	11:07	415 ± 17	387 ± 22	388 ± 34	380 ± 21	9.8 ± 3.2	10.0 ± 5.0	3.6 ± 2.7	6.0 ± 3.0	0.95 ± 0.11	0.51 ± 0.15	0.19 ± 0.09	0.25 ± 0.09
11:12	11:26	384 ± 17	421 ± 21	384 ± 29	398 ± 25	17.3 ± 6.8	5.5 ± 2.1	3.9 ± 2.5	4.3 ± 2.3	0.83 ± 0.21	0.60 ± 0.07	0.18 ± 0.09	0.29 ± 0.07
11:28	11:41	380 ± 17	448 ± 25	393 ± 26	510 ± 36	20.2 ± 7.8	3.4 ± 1.4	3.0 ± 1.7	0.8 ± 0.4	0.87 ± 0.23	0.62 ± 0.06	0.18 ± 0.06	0.39 ± 0.02
11:46	11:59	437 ± 25	506 ± 28	491 ± 43	425 ± 26	5.7 ± 2.4	1.4 ± 0.5	0.7 ± 0.4	2.6 ± 1.2	0.85 ± 0.11	0.67 ± 0.03	0.28 ± 0.02	0.31 ± 0.04
12:00	12:13	364 ± 27	500 ± 35	628 ± 64	495 ± 38	19.1 ± 12.8	1.4 ± 0.6	0.1 ± 0.1	0.6 ± 0.3	0.53 ± 0.53	0.59 ± 0.04	0.24 ± 0.01	0.26 ± 0.02
12:18	12:31	477 ± 35	460 ± 26	439 ± 38	415 ± 28	2.2 ± 1.1	2.7 ± 1.1	1.2 ± 0.8	2.8 ± 1.5	0.68 ± 0.09	0.60 ± 0.05	0.19 ± 0.04	0.27 ± 0.06
12:33	12:46	402 ± 27	407 ± 19	448 ± 32	453 ± 22	8.3 ± 4.5	7.6 ± 2.8	1.1 ± 0.6	2.0 ± 0.7	0.59 ± 0.23	0.62 ± 0.08	0.19 ± 0.03	0.40 ± 0.02
12:51	13:03	391 ± 32	394 ± 26	448 ± 30	452 ± 20	8.3 ± 5.8	9.1 ± 5.1	1.2 ± 0.6	2.0 ± 0.7	0.46 ± 0.35	0.54 ± 0.16	0.21 ± 0.03	0.41 ± 0.02
13:05	13:18	423 ± 29	485 ± 29	495 ± 37	436 ± 22	5.3 ± 2.9	1.9 ± 0.8	0.6 ± 0.3	2.6 ± 1.0	0.60 ± 0.17	0.64 ± 0.04	0.23 ± 0.02	0.37 ± 0.03
13:23	13:36	420 ± 32	505 ± 28	483 ± 46	512 ± 33	4.9 ± 2.9	1.5 ± 0.5	0.5 ± 0.3	0.8 ± 0.3	0.52 ± 0.19	0.69 ± 0.03	0.17 ± 0.03	0.38 ± 0.02
Co-average*	404 ± 11	436 ± 9	460 ± 11	436 ± 10	9.2 ± 2.1	4.0 ± 0.6	0.9 ± 0.2	2.1 ± 0.4	0.70 ± 0.09	0.60 ± 0.02	0.20 ± 0.01	0.31 ± 0.01	0.31 ± 0.01
Mean value	409 ± 8	451 ± 9	460 ± 12	441 ± 9	10.1 ± 1.9	4.5 ± 0.8	1.6 ± 0.4	2.6 ± 0.5	0.70 ± 0.08	0.61 ± 0.03	0.21 ± 0.02	0.32 ± 0.02	0.32 ± 0.02

Table 4

As Table 2, but for data obtained on 21 April 2013.

4.1 Conjugate northern and southern aurorae

In Tables 2 - 4, the co-added average temperatures in the NMO are lower than in the SMO on each day. The individually derived H_3^+ temperatures for the spectral images are shown in Figure 6, together with dashed lines which indicate the average value of all of the data points (i.e. not the same averages as in Tables 2 - 4, but the differences between the two are very small). *O'Donoghue et al.* [2014] found that over a period of ∼2 hours the southern main auroral oval was on average 56 K hotter than its northern counterpart. This was attributed to the north-south asymmetry in magnetic field strength which leads to an overall larger total heating rate in the south, with the caveat being that their dataset was small and considered a snapshot of events at that time (in April 2011). In this work we have three similar snapshots over consecutive days, each appearing to support to the previous result that the SMO is warmer than the NMO by 10's of K when measured simultaneously for each of the days.

A summary of the effective average H_3^+ temperatures observed to date is presented in Table 5. The considerable year-to-year variability is difficult to attribute to seasonal or solar cycle effects, such that variability on shorter time scales of minutes, hours, and days should be considered. This is discussed in Subsection 4.3 where we outline a likely reason for the several 10's of Kelvin variability seen in the NMO temperatures.

Tables 2 - 4 also show that column densities are higher in the northern main oval than the southern by on average a factor of ∼3, as shown in Figure 7, though these have large uncertainties associated with them. A possible reason for a higher northern column density is the additional solar illumination in the north compared with that incident at the south; this yields a higher ionisation rate of H_2 and therefore an increase in H_3^+ production. Such an effect has previously been observed and also demonstrated using the 1-D Saturn Thermosphere Ionosphere Model (STIM) by *O'Donoghue et al.* [2014]. All but one pair of values is in agreement

Date	T_{SMO} (K)	T_{NMO} (K)	T_{NPC} (K)	T_{NMMO} (K)	Source
Sept. 1999	380 ±70	-	-	-	NASA IRTF, *Melin et al.* [2007]
Feb. 2004	420 ±70	-	-	-	NASA IRTF, *Melin et al.* [2007]
July 2007	590 ±50	-	-	-	Cassini VIMS, *Stallard et al.* [2012a]
Jan. 2009	410 ±85	-	-	-	Cassini VIMS, *Lamy et al.* [2013]
April 2011	583 ±13	527 ±18	-	-	Keck, *O'Donoghue et al.* [2014]
April 2013	444 ±18	416 ±18	433 ±13	466 ±16	Keck, This work

Table 5

The average temperatures of Saturn's auroral regions obtained between 1999 and the 2013.

with this trend; at ∼12 UT on April 19 in panel (a) the southern column density is higher. The densities vary by up to an order of magnitude from day-to-day, with the major deviations outside the ranges of uncertainty seen in panel (c).

The variability in column density is likely to be associated with changes in the energy flux that is incident on the ionosphere, e.g. increased particle precipitation provides more ionization and thus more H_3^+. Similar variability in the energy flux has been attributed to variations in H_3^+ aurora before using Cassini VIMS data [*Badman et al.* 2012b;a], and in patches of intense UV emissions from H and H_2 [*Nichols et al.* 2009; *Grodent et al.* 2011; *Meredith et al.* 2013]. An influx of particles at local noon may be the result of dayside reconnection events which occur when the interplanetary magnetic field (IMF) is orientated northward, leading to the opening of closed planetary magnetic field lines to the solar wind, causing a planetward influx of solar particles [*Radioti et al.* 2011; 2013; *Badman et al.* 2013; *Meredith et al.* 2014; *Belenkaya et al.* 2014]. Alternatively, new parts of the main auroral oval, differing in their levels of activity, may be rotating into view on the spectrograph slit. No correlations are found between the northern and southern main ovals, despite sharing common (closed) magnetic field lines, and this is consistent with recent Hubble Space Telescope (HST) observations which showed patches of UV emission in the auroral main oval are present in one hemisphere, but absent from the

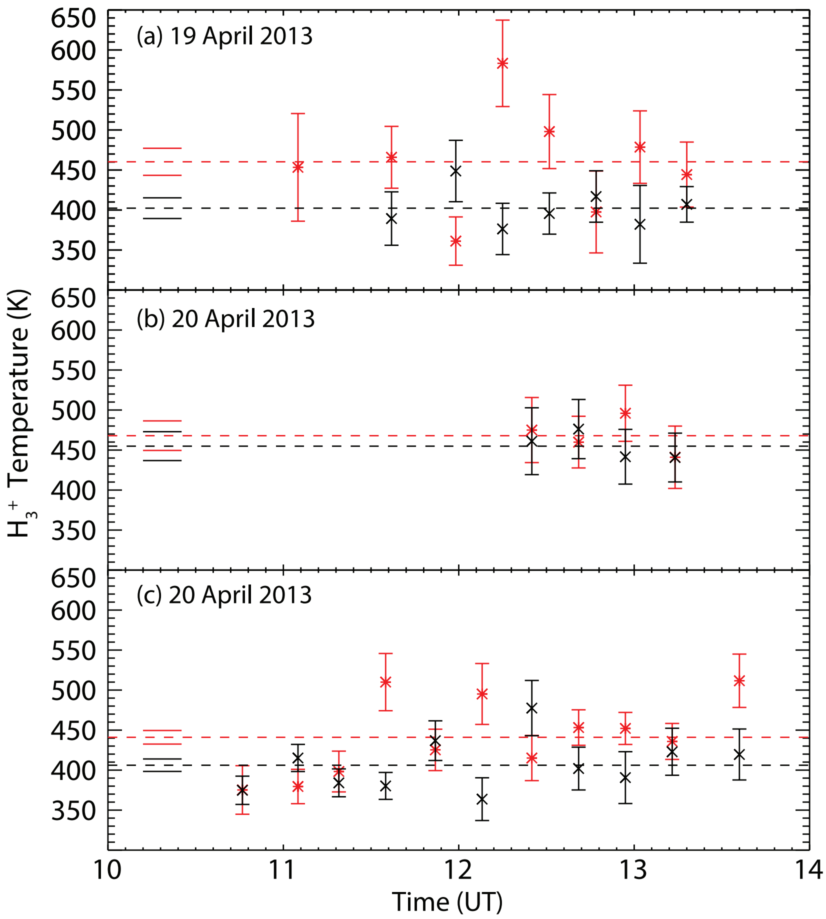

Fig. 6. **NMO and SMO H_3^+ temperature as a function of observation time.** The three panels show H_3^+ temperatures as a function of time for the three nights of observations as indicated. The NMO values are shown as the black crosses, while the SMO values are shown as the red asterisks. The uncertainties listed are 1-sigma and arise from the S/N of the spectral fit. Note that the northern main oval temperature of 994 ±900 K (in the first row of Table 2) is not shown in panel (a), as it is assumed to be unphysical (this was possibly due to a passing cirrus cloud, reducing the S/N). The black and red dashed horizontal lines show the average temperature of all the plotted data points for north and south, respectively, with associated 1-sigma uncertainties above and below shown as short solid lines.

magnetically conjugate location in the other [*Meredith et al.* 2014].

The total emission shown in Tables 2 - 4 and Figure 8 is higher in the NMO for nearly all data points compared to the SMO - a similar trend is seen in column density, but in this case

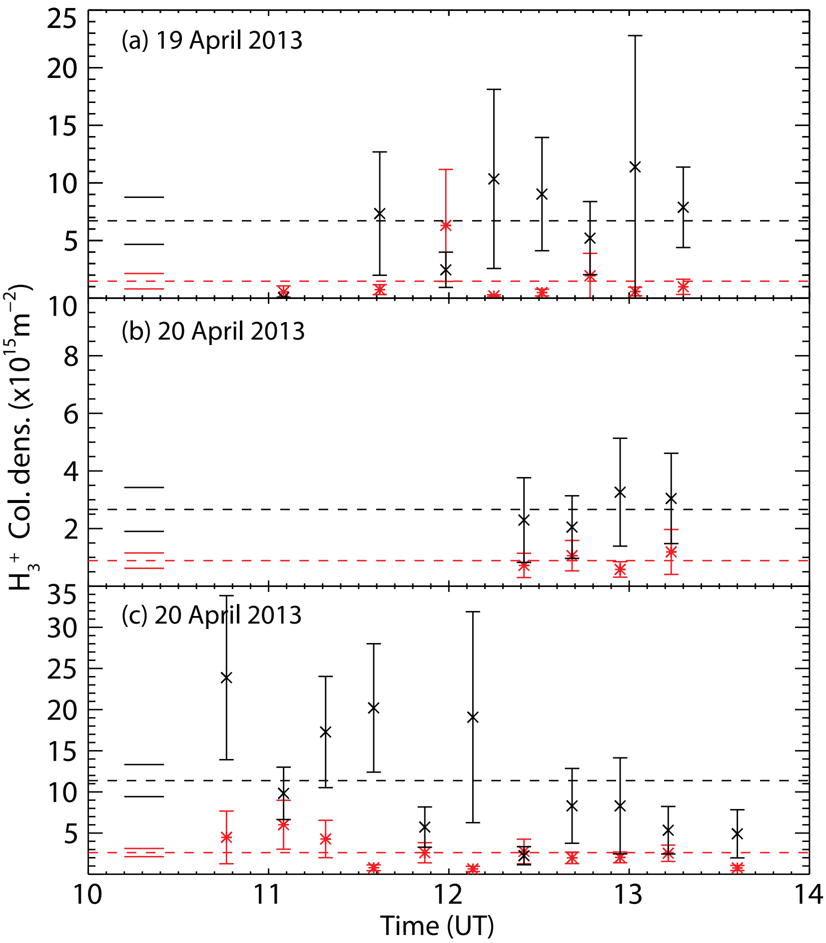

Fig. 7. **NMO and SMO H_3^+ column densities as a function of time.** The figure format is the same as Figure 6.

with smaller uncertainties. The total emission is a direct measure of H_3^+ cooling to space, so it might be argued that in the NMO, the larger quantity of H_3^+ would have led to a higher rate of thermospheric cooling, which in turn has led to lower temperatures. However, the observations by *O'Donoghue et al.* [2014] are a counter example in that high densities are associated with low total emissions, so this is not an obvious cause. Furthermore, the global circulation modeling (GCM) results of *Mueller-Wodarg et al.* [2012] of Saturn during equinoctial conditions show that H_3^+ acts only as a minor coolant in the thermosphere. The major heating mechanism in the auroral thermosphere is Joule heating, whilst adiabatic cooling and advection are the major heat sinks in the upper polar atmosphere. The densities observed here are similar to *O'Donoghue et al.* [2014] and are within the 1 to 12 $\times 10^{15}\mathrm{m}^{-2}$ range of values modeled by

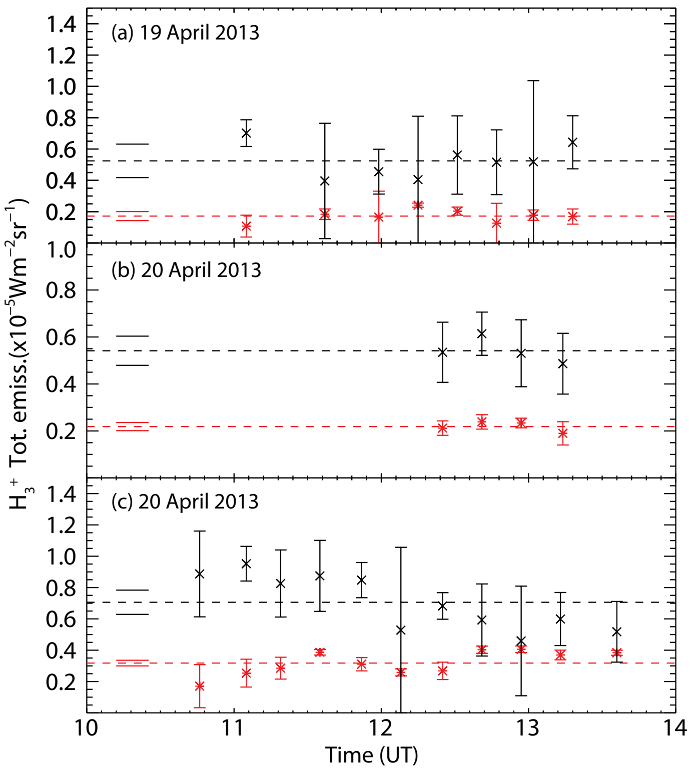

Fig. 8. **NMO and SMO H_3^+ total emission as a function of time.** The figure format is the same as Figure 6.

Mueller-Wodarg et al. [2012]. There are no obvious trends found here that lead us to conclude a dependence of H_3^+ parameters with system III CML. The NMO and SMO individually show sporadic variability of several 10's of K throughout all CML's, indicating little or no observable relationship.

4.2 Relationships between the noon, polar cap and midnight aurorae

In Figure 9 we show the H_3^+ parameters of all of the four previously mentioned spatial regions (as shown in Figure 3) as a function of system III longitude (CML). Before continuing we note that the nearby components of the north are close together and therefore subject to latitudinal smearing, i.e. cross-contamination, even though gaps were left between the target areas. This is due to (mainly) atmospheric scintillation/seeing effects and telescope movement during spectral image exposures. However, comparison between the northern main oval and midnight are separated significantly enough that these effects are negligible. First, we find that there are no obvious trends leading us to conclude a dependence of H_3^+ parameters with CML. The northern and southern main ovals individually show sporadic variability of several 10's of K throughout all CMLs, indicating little or no observable relationship. However, the northern main oval (black crosses) total emission and column density do appear to have significantly higher values than the average near 50-100° CML, and this will be discussed in the next section. A lack of an obvious pattern is perhaps unsurprising as there are no known CML dependencies of Saturn's magnetic field. Our interests here therefore lie mainly in the average behavior of each region from the combined three days of observations. The CMLs for the northern midnight main oval are shifted by 180 degrees as they are on the 'night' (but sunlit) side of the planet, whilst the northern polar cap (which straddles both sides) uses northern main oval CMLs. The effective column integrated H_3^+ temperature is on average 465 K at midnight, 53 K greater than in the main oval. Column density averages are 1×10^{15} m^{-2} at midnight and 8.6×10^{15} m^{-2} at noon, similar to values produced through modeling efforts by *Moore et al.* [2004], though these were produced by solar EUV alone (i.e., non-auroral conditions). Finally, the total emission is 0.6×10^{-5} $Wm^{-2}sr^{-1}$ at noon and 0.18×10^{-5} $Wm^{-2}sr^{-1}$ at northern midnight. The polar aurora temperature is 439 K on average, whilst the column density and total emission values are 45% and 75%, respectively, of the northern main oval values, indicating that perhaps this region is contaminated by its neighbors through the seeing effects mentioned above. Southern parameters have already been discussed in the context of their northern counterparts, but appear to be most similar to the northern midnight main oval.

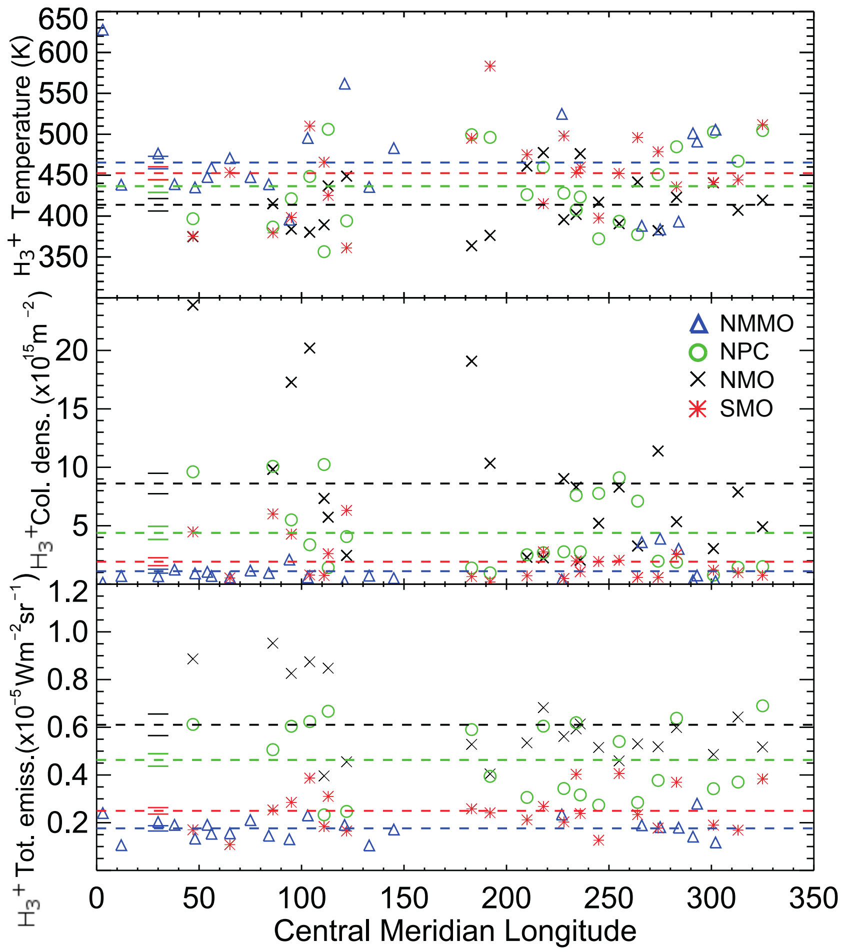

Fig. 9. **Northern H_3^+ properties as a function of Saturn system III CML.** Here we show the northern H_3^+ temperature, column density and total emission in panels (a), (b) and (c), respectively as a function of central meridian longitude. The different regions of interest are the northern main oval (black crosses), polar cap (green circles), midnight aurorae (blue triangles) and southern main oval (red asterisks). The average values for each are shown as dashed horizontal lines with 1-sigma uncertainty bars as short solid lines above and below to the left of the figure. The northern values at ∼62° CML are not shown and not included in the calculation of average values due to high uncertainties described earlier.

Mueller-Wodarg et al. [2012] modeled Saturn's upper atmosphere for equinoctial conditions, including the effects of solar radiation, magnetospheric electron precipitation and the contribution to the total heating rate provided by Joule heating and ion drag. The authors calculated auroral H_3^+ temperatures (at 78° southern latitude) of ~419 K at midnight, 1 - 2 K warmer than at noon. Although these temperatures are similar in absolute terms to those observed in this work, the difference between the noon and midnight sectors is clearly much greater here (55 K); the reason for this midnight temperature enhancement is unknown. The column density, on the other hand, was modeled to be $\sim 12 \times 10^{15}$ m^{-2} at noon, compared with $\sim 1 \times 10^{15}$ m^{-2} at midnight, similar to that observed here. The northern column emission is a factor of ~3 higher at noon compared to midnight in our observations, yet a factor of 15 different in the above model. There are thus some areas of agreement between the model of *Mueller-Wodarg et al.* [2012] and the observations presented here, though the relative noon-midnight differences between parameters are quite large. Cross-contamination between the polar cap and the main oval due to atmospheric seeing may play a role in the observation-model factor differences between noon and midnight. The higher noon density and emission is likely to be driven by the higher levels of 10 keV electron flux there, in accordance with the predicted maximum flux at 08:00 Saturn local time (SLT), which then diminishes to a minimum near midnight [*Lamy et al.* 2009]. The parameters obtained in the polar region shown by the green circles in Figure 9 appear essentially to be the average of the other northern values. The activity here could be maintained by transport from the midnight and noon sectors, as well as be modulated by particle precipitation along open field lines which connect the planet directly to the solar wind.

4.3 Variation of northern main oval H_3^+ with northern PPO phase

In the last section, although there was no clear organisation with CML, there were a number of high density and emission values in the northern main oval at around 50-100° CML in Figure 9. In addition, this is a region in which we have a complete view of the 8 - 20° co-latitudes that define it (compared with the limited southern main oval field of view of 18 - 22°), so it is an ideal place to explore any short-term variability; in particular, that imposed by the planetary period oscillations of the magnetic field. In the four panels of Figure 10 we plot each of the NMO H_3^+ parameters from all three days as a function of PPO phase, Ψ_N, between 0° and 360°. In Figure 10 panel (a) we plot the H_3^+ Q(1,0) line intensity versus the northern PPO phase, and we find a factor of ~2 higher intensity between 90 - 135°. The line intensity is a useful metric for the overall activity of H_3^+ as it is directly observed and is a function of both temperature and density. The location of the center of the fitted Gaussian distribution curve (the peak) shown over-plotted in black is located at 115° and has a FWHM of 44°. Figure 10 panel (b) shows the NMO temperature against northern PPO phase, and this anti-correlates with the column density shown in panel (c) with a Spearman's rank coefficient r = -0.95 (with a probability that these values are uncorrelated of $p < 0.01$). This and other correlations between H_3^+ parameters are given in Table 6. The column density Gaussian curve peaks at 118° and has a FWHM of 49°- almost identical in location to the Q(1,0) line peak. In panel (d) the total emission the Gaussian curve peaks at 114° with a FWHM of 40°.

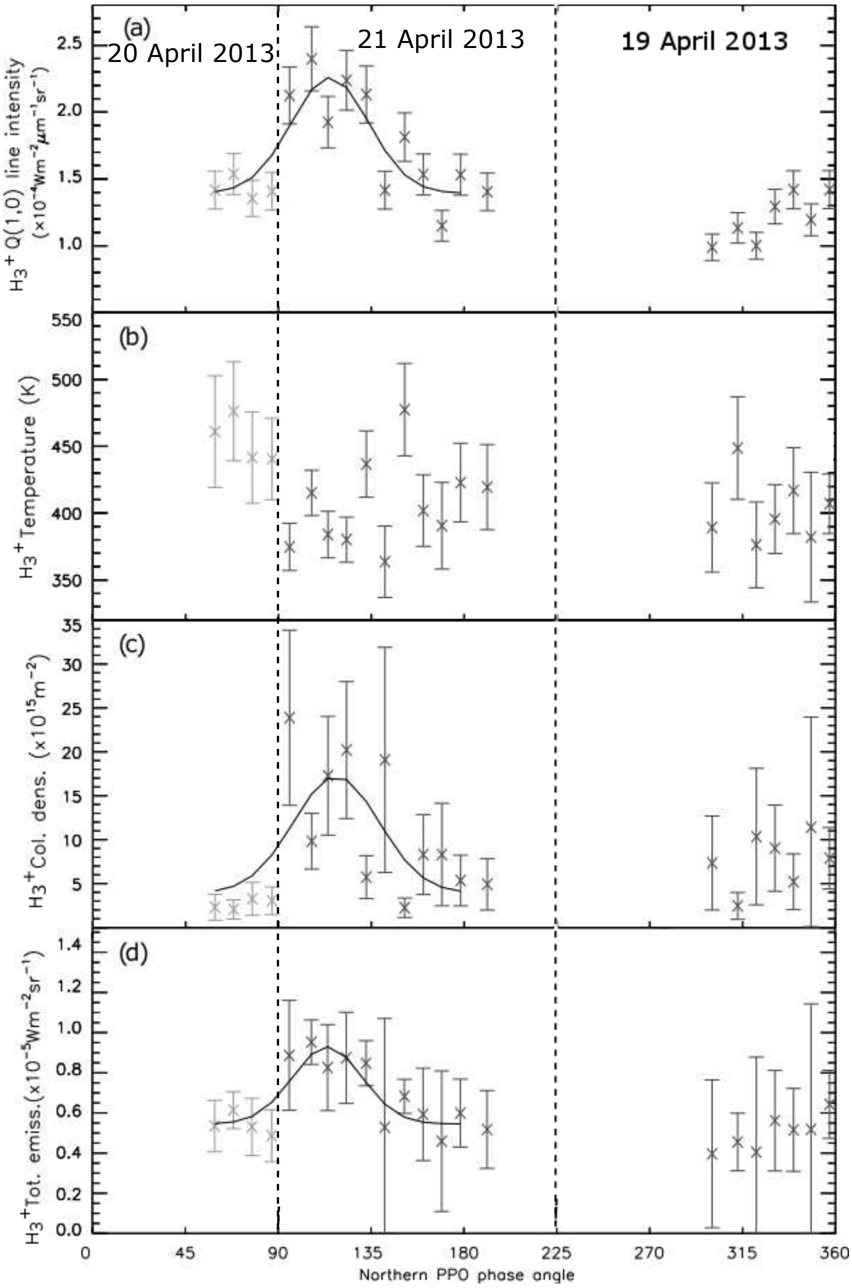

Fig. 10. **NMO H_3^+ parameters as a funciton of northern PPO phase.** Here we show the northern main oval results from the three days of this study as a function of the PPO phase angle described in the main text. The following H_3^+ parameters are shown in each of the four panels: (a) Q(1,0) line intensity, (b) temperature, (c) column density and (d) total emission.

The theoretical peak particle precipitation is thought to occur at $\Psi_N = 90^\circ$ as discussed in the introduction, so the above locations are some 25 degrees later on in PPO phase (1 hour and 40 minutes earlier in Saturn LT). First we note that the phase model is accurate to

H_3^+ parameter	Temperature	Column density	Total emission
Q(1,0) intensity	r = -0.04 (p = 0.85)	r = 0.25 (p = 0.23)	r =0.79 (p <0.01)
Total emission	r = 0.08 (p = 0.73)	r = 0.17 (p = 0.43)	-
Column density	r = -0.95 (p < 0.01)	-	-

Table 6

Spearman's rank correlation coefficients between H_3^+ parameters when arranged in order of PPO phase.

approximately ±10°, so this may account for some of the deviation from expectations [*Provan et al.* 2014]. Second, the FWHM is approximately 44° for the peaks above, a considerable spread in longitude; a reason for this may be the fact that our measurements are based on spectral image exposures that are ∼15 minutes in length and thus accuracy is limited to approximately ±5° in PPO phase. Finally, the position of the starting location/time of the measured peak in density and emission could be shifted forward due to the chemical lifetime of H_3^+ being approximately 100 - 1000 seconds [*Badman et al.* 2014]. The lifetime of H_3^+ is also likely to extend the end location/time of the Gaussian profile. Here by combining the recombination rate 17.32 $\times 10^{-7}$cm^{3}s^{-1} from *Moses and Bass* [2000] with typical values for the temperature and number density in the auroral region at these altitudes, 450 K and 1×10^4cm^{-3} [*Mueller-Wodarg et al.* 2012], we obtain an H_3^+ lifetime of ∼1230 seconds. These factors when combined could result in the Gaussian profile being shifted by up to 20 degrees CML/phase angle later, so the results herein are not inconsistent with the predicted periodic enhancement in electron influx.

We have indicated the results from different days in the panels of Figure 10. The majority of the curvature of the profile coming from the data taken on 21 April. As this dataset has no overlapping PPO phase data from the different days, we cannot rule out that the observed patterns are due to an enhancement in particle precipitation driven by other mechanisms. For example, an interplanetary magnetic field (IMF) pointing northward can lead to magnetic reconnection at low latitudes, such that planetary field lines become open and connect with the solar wind [*Badman et al.* 2013]. A combination of longer observations and overlapping data over the same PPO phases are required in order to definitively confirm the findings here.

Interestingly, the temperature appears to be lowest where the influx of charged particles is highest. This could be in part due to a slight cooling effect of H_3^+ whereby it radiates heat to space, although modeling work has shown such cooling is minor compared to other processes like adiabatic cooling [*Mueller-Wodarg et al.* 2012]. Given the uncertainties in column density, it is possible that the anti-correlations are not entirely physical and are tainted by the least-squares fitting routine employed herein [*Melin et al.* 2014]. However, the trends in Figure 10 are arrived at independently from the fitting routine in panel (a) and through a combined temperature and column density in panel (d), thus we have shown multiple instances of possible H_3^+-PPO phase dependance.

Analysis of the other regions (SMO, NPC, NMMO) did not yield similar correlations (or at least, not as strongly) to that of the NMO, although those are regions of lower spatial resolution and higher cross-latitude contamination due to seeing effects. Given the significant variability seen here, it is important that similar future research include the contributions made by the PPO perturbation.

5 Summary

On April 19, 20 and 21, the ground-based Keck telescope was employed to simultaneously measure H_3^+ parameters (temperature, density and total emission) in four specific regions of Saturn's ionosphere/thermosphere: 1) the northern noon region of the main auroral oval; 2) the northern midnight main oval; 3) the northern polar cap and 4) the southern noon main oval. In these locations, the 115 minutes of captured exposures on Saturn were used to derive ninety-two

H_3^+ temperatures, column densities and total emissions spread over timescales of both hours and days, and therefore over a wide range of Saturn system III longitudes (CMLs) and planetary period oscillation (PPO) phase angles. We have found that column integrated thermospheric temperatures in the northern main oval are cooler than their southern counterparts by tens of K on average. Although the northern aurorae is at times hotter than the south for some individual measurements, this work lends support the hypothesis that the total thermospheric heating rate (Joule heating and ion drag) is inversely proportional to magnetic field strength, as discussed by *O'Donoghue et al.* [2014]. The midnight portion of the oval is on average 55 K warmer than it is at noon, but the cause for this is unclear. The main oval column integrated H_3^+ density and emission is lower at northern midnight than it is at noon, in agreement with a peak in the electron influx at 08:00 Saturn local time and a minimum flux at midnight. When the northern main oval parameters of H_3^+ are ordered into the northern PPO phase we see a large peak in H_3^+ density and emission at $\sim$115° northern phase, with a full-width at half-maximum (FWHM) of $\sim$44°. We find that these peaks are most likely due to the expected theoretical enhancement in the influx of electrons associated with the PPO phase at 90°. A combination of the H_3^+ reaction time to the influx due to ion chemistry timescales, the $\pm$10° uncertainty in the location of a given PPO phase and the lifetime of H_3^+ are likely to be partly responsible for the observed peaks in H_3^+ density and emission occurring later in time (forward in phase) of the expected precipitation location.

Acknowledgements The data presented herein were obtained at the W.M. Keck Observatory, which is operated as a scientific partnership among the California Institute of Technology, the University of California, and NASA. We are particularly grateful to the observing staff in both Waimea and Mauna Kea for their kind assistance and we praise their ability to seemingly clear the sky of clouds whenever we observe. The observations were made to support the Cassini auroral campaign in April 2013. Discussions within the international team lead by Tom Stallard on 'Comparative Jovian Aeronomy' have greatly benefited this work; this was hosted by the International Space Science Institute (ISSI). The UK Science and Technology Facilities Council (STFC) supported this work through the Studentship Enhancement Programme (STEP) for J.O'D. and consolidated grant support for T.S.S., S.W.H.C. and H.M., whilst S.V.B. was supported by a Royal Astronomical Society Research Fellowship. This material is based upon work supported by the National Aeronautics and Space Administration under Grant No. 9500303356 issued through the Planetary Astronomy Program for L.M. and J.O'D. We thank the NASA Planetary Data System (PDS) for planetary parameter and viewing geometry data.

References

Andrews, D. J., E. J. Bunce, S. W. H. Cowley, M. K. Dougherty, G. Provan, and D. J. Southwood (2008), Planetary period oscillations in Saturn's magnetosphere: Phase relation of equatorial magnetic field oscillations and Saturn kilometric radiation modulation, *J. Geophys. Res. (Space Physics)*, *113*, A09205, doi:10.1029/2007JA012937.

Andrews, D. J., A. J. Coates, S. W. H. Cowley, M. K. Dougherty, L. Lamy, G. Provan, and P. Zarka (2010), Magnetospheric period oscillations at Saturn: Comparison of equatorial and high-latitude magnetic field periods with north and south Saturn kilometric radiation periods, *J. Geophys. Res. (Space Physics)*, *115*, A12252, doi:10.1029/2010JA015666.

Badman, S. V., S. W. H. Cowley, J.-C. Gérard, and D. Grodent (2006), A statistical analysis of the location and width of Saturn's southern auroras, *Ann. Geophys.*, *24*, 3533–3545, doi:10.5194/angeo-24-3533-2006.

Badman, S. V., D. J. Andrews, S. W. H. Cowley, L. Lamy, G. Provan, C. Tao, S. Kasahara, T. Kimura, M. Fujimoto, H. Melin, T. Stallard, R. H. Brown, and K. H. Baines (2012a), Rotational modulation and local time dependence of Saturn's infrared H_3^+ auroral intensity, *J. Geophys. Res.*, *117*, A09228, doi:10.1029/2012JA017990.

Badman, S. V., N. Achilleos, C. S. Arridge, K. H. Baines, R. H. Brown, E. J. Bunce, A. J.

Coates, S. W. H. Cowley, M. K. Dougherty, M. Fujimoto, G. Hospodarsky, S. Kasahara, T. Kimura, H. Melin, D. G. Mitchell, T. Stallard, and C. Tao (2012b), Cassini observations of ion and electron beams at Saturn and their relationship to infrared auroral arcs, *J. Geophys. Res.*, *117*, A01211, doi:10.1029/2011JA017222.

Badman, S. V., A. Masters, H. Hasegawa, M. Fujimoto, A. Radioti, D. Grodent, N. Sergis, M. K. Dougherty, and A. J. Coates (2013), Bursty magnetic reconnection at Saturn's magnetopause, *Geophys. Res. Lett.*, *40*, 1027–1031, doi:10.1002/grl.50199.

Badman, S. V., G. Branduardi-Raymont, M. Galand, S. L. G. Hess, N. Krupp, L. Lamy, H. Melin, and C. Tao (2014), Auroral Processes at the Giant Planets: Energy Deposition, Emission Mechanisms, Morphology and Spectra, *Space Sci. Rev.*, doi:10.1007/s11214-014-0042-x.

Barrow, D. J., and K. I. Matcheva (2013), Modeling the effect of atmospheric gravity waves on Saturn's ionosphere, *Icarus*, *224*, 32–42, doi:10.1016/j.icarus.2013.01.027.

Belenkaya, E. S., S. W. H. Cowley, C. J. Meredith, J. D. Nichols, V. V. Kalegaev, I. I. Alexeev, O. G. Barinov, W. O. Barinova, and M. S. Blokhina (2014), Magnetospheric magnetic field modelling for the 2011 and 2012 HST Saturn aurora campaigns - implications for auroral source regions, *Ann. Geophys.*, *32*, 689–704, doi:10.5194/angeo-32-689-2014.

Brown, R. H., K. H. Baines, G. Bellucci, J.-P. Bibring, B. J. Buratti, F. Capaccioni, P. Cerroni, R. N. Clark, A. Coradini, D. P. Cruikshank, P. Drossart, V. Formisano, R. Jaumann, Y. Langevin, D. L. Matson, T. B. McCord, V. Mennella, E. Miller, R. M. Nelson, P. D. Nicholson, B. Sicardy, and C. Sotin (2004), The Cassini Visual And Infrared Mapping Spectrometer (Vims) Investigation, *Space Science Reviews*, *115*, 111–168, doi:10.1007/s11214-004-1453-x.

Bunce, E. J., C. S. Arridge, J. T. Clarke, A. J. Coates, S. W. H. Cowley, M. K. Dougherty, J.-C. Gérard, D. Grodent, K. C. Hansen, J. D. Nichols, D. J. Southwood, and D. L. Talboys (2008), Origin of Saturn's aurora: Simultaneous observations by Cassini and the Hubble Space Telescope, *J. Geophys. Res. (Space Physics)*, *113*, A09209, doi:10.1029/2008JA013257.

Burton, M. E., M. K. Dougherty, and C. T. Russell (2010), Saturn's internal planetary magnetic field, *J. Geophys. Res.*, *37*, L24105, doi:10.1029/2010GL045148.

Carbary, J. F. (2012), The morphology of Saturn's ultraviolet aurora, *J. Geophys. Res. (Space Physics)*, *117*, A06210, doi:10.1029/2012JA017670.

Cowley, S. W. H., and E. J. Bunce (2003), Corotation-driven magnetosphere-ionosphere coupling currents in Saturn's magnetosphere and their relation to the auroras, *Annales Geophysicae*, *21*, 1691–1707, doi:10.5194/angeo-21-1691-2003.

Cowley, S. W. H., E. J. Bunce, and J. M. O'Rourke (2004), A simple quantitative model of plasma flows and currents in Saturn's polar ionosphere, *J. Geophys. Res.*, *109*, A05212, doi:10.1029/2003JA010375.

Grodent, D., J. H. Waite, Jr., and J.-C. Gérard (2001), A self-consistent model of the Jovian auroral thermal structure, *J. Geophys. Res.*, *106*, 12,933–12,952, doi:10.1029/2000JA900129.

Grodent, D., J. Gustin, J.-C. Gérard, A. Radioti, B. Bonfond, and W. R. Pryor (2011), Small-scale structures in Saturn's ultraviolet aurora, *J. Geophys. Res. (Space Physics)*, *116*, A09225, doi:10.1029/2011JA016818.

Gurnett, D. A., A. Lecacheux, W. S. Kurth, A. M. Persoon, J. B. Groene, L. Lamy, P. Zarka, and J. F. Carbary (2009), Discovery of a north-south asymmetry in Saturn's radio rotation period, *Geophys. Res. Lett.*, *36*, L16102, doi:10.1029/2009GL039621.

Hunt, G. J., S. W. H. Cowley, G. Provan, E. J. Bunce, I. I. Alexeev, E. S. Belenkaya, V. V. Kalegaev, M. K. Dougherty, and A. J. Coates (2014), Field-aligned currents in Saturns southern nightside magnetosphere: Sub-corotation and planetary period oscillation components., *J. Geophys. Res. (submitted)*.

Kaiser, M. L., M. D. Desch, J. W. Warwick, and J. B. Pearce (1980), Voyager detection of nonthermal radio emission from Saturn, *Science*, *209*, 1238–1240, doi: 10.1126/science.209.4462.1238.

Kao, L., T. Oka, S. Miller, and J. Tennyson (1991), A table of astronomically important ro-vibrational transitions for the H3(+) molecular ion, *ApJS*, *77*, 317–329, doi:10.1086/191606.

Koskinen, T. T., B. R. Sandel, R. V. Yelle, F. J. Capalbo, G. M. Holsclaw, W. E. McClintock, and S. Edgington (2013), The density and temperature structure near the exobase of Saturn from Cassini UVIS solar occultations, *Icarus*, *226*, 1318–1330, doi:10.1016/j.icarus.2013.07.037.

Lam, H. A., N. Achilleos, S. Miller, J. Tennyson, L. M. Trafton, T. R. Geballe, and G. E. Ballester (1997), A Baseline Spectroscopic Study of the Infrared Auroras of Jupiter, *Icarus*, *127*, 379–393, doi:10.1006/icar.1997.5698.

Lamy, L., B. Cecconi, R. Prangé, P. Zarka, J. D. Nichols, and J. T. Clarke (2009), An auroral oval at the footprint of Saturn's kilometric radio sources, colocated with the UV aurorae, *J. Geophys. Res. (Space Physics)*, *114*, A10212, doi:10.1029/2009JA014401.

Lamy, L., R. Prangé, W. Pryor, J. Gustin, S. V. Badman, H. Melin, T. Stallard, D.-G. Mitchell, and P. C. Brandt (2013), Multispectral simultaneous diagnosis of Saturn's aurorae throughout a planetary rotation, *J. Geophys. Res. (Space Physics)*, *118*, 4817–4843, doi:10.1002/jgra.50404.

McLean, I. S., E. E. Becklin, O. Bendiksen, G. Brims, J. Canfield, D. F. Figer, J. R. Graham, J. Hare, F. Lacayanga, J. E. Larkin, S. B. Larson, N. Levenson, N. Magnone, H. Teplitz, and W. Wong (1998), Design and development of NIRSPEC: a near-infrared echelle spectrograph for the Keck II telescope, in *Society of Photo-Optical Instrumentation Engineers (SPIE) Conference Series*, *Society of Photo-Optical Instrumentation Engineers (SPIE) Conference Series*, vol. 3354, edited by A. M. Fowler, pp. 566–578.

Melin, H. (2006), Comparative Aeronomy of the Upper Atmospheres of the Giant Planets, *University College London*.

Melin, H., S. Miller, T. Stallard, L. M. Trafton, and T. R. Geballe (2007), Variability in the H_3^+ emission of Saturn: Consequences for ionisation rates and temperature, *Icarus*, *186*, 234–241, doi:10.1016/j.icarus.2006.08.014.

Melin, H., T. Stallard, S. Miller, J. Gustin, M. Galand, S. V. Badman, W. R. Pryor, J. O'Donoghue, R. H. Brown, and K. H. Baines (2011), Simultaneous Cassini VIMS and UVIS observations of Saturn's southern aurora: Comparing emissions from H, H_2 and H_3^+ at a high spatial resolution, *Geophysical Research Letters*, *38*, L15203, doi: 10.1029/2011GL048457.

Melin, H., T. S. Stallard, J. O'Donoghue, S. V. Badman, S. Miller, and J. S. D. Blake (2014), On the anticorrelation between H_3^+ temperature and density in giant planet ionospheres, *Mon. Not. R. Astron. Soc.*, *438*, 1611–1617, doi:10.1093/mnras/stt2299.

Meredith, C., S. W. H. Cowley, K. C. Hansen, J. D. Nichols, and T. K. Yeoman (2013), Simultaneous conjugate observations of small-scale structures in Saturn's dayside ultraviolet auroras - implications for physical origins, *J. Geophys. Res. (Submitted)*.

Meredith, C. J., I. I. Alexeev, S. V. Badman, E. S. Belenkaya, S. W. H. Cowley, M. K. Dougherty, V. V. Kalegaev, G. R. Lewis, and J. D. Nichols (2014), Saturn's dayside ultraviolet auroras: Evidence for morphological dependence on the direction of the upstream interplanetary magnetic field, *J. Geophys. Res. (Space Physics)*, *119*, 1994–2008, doi:10.1002/2013JA019598.

Miller, S., R. D. Joseph, and J. Tennyson (1990), Infrared emissions of H3(+) in the atmosphere of Jupiter in the 2.1 and 4.0 micron region, *Astrophys. J.*, *360*, L55–L58, doi:10.1086/185811.

Miller, S., T. Stallard, C. Smith, and et al. (2006), H_3^+: the driver of giant planet atmospheres, *Phil. Trans. Roy. Soc. London.*, *364*, 3121–3137, doi:10.1098/rsta.2006.1877.

Miller, S., T. Stallard, H. Melin, and J. Tennyson (2010), H_3^+ cooling in planetary atmospheres, *Faraday Discussions*, *147*, 283, doi:10.1039/c004152c.

Moore, L., M. Galand, I. Mueller-Wodarg, R. Yelle, and M. Mendillo (2008), Plasma temperatures in Saturn's ionosphere, *J. Geophys. Res. (Space Physics)*, *113*, A10306, doi: 10.1029/2008JA013373.

Moore, L. E., M. Mendillo, I. C. F. Müller-Wodarg, and D. L. Murr (2004), Modeling of global variations and ring shadowing in Saturn's ionosphere, *Icarus*, *172*, 503–520, doi: 10.1016/j.icarus.2004.07.007.

Moses, J. I., and S. F. Bass (2000), The effects of external material on the chemistry and structure of Saturn's ionosphere, *J. Geophys. Res.*, *105*, 7013–7052, doi:10.1029/1999JE001172.

Mueller-Wodarg, I. C. F., L. Moore, M. Galand, S. Miller, and M. Mendillo (2012), Magnetosphere-atmosphere coupling at Saturn: 1 - Response of thermosphere and ionosphere to steady state polar forcing, *Icarus*, *221*, 481–494, doi:10.1016/j.icarus.2012.08.034.

Neale, L., S. Miller, and J. Tennyson (1996), Spectroscopic Properties of the H_3^+ Molecule: A New Calculated Line List, *The Astrophysical Journal*, *464*, 516, doi:10.1086/177341.

Nichols, J. D., S. V. Badman, E. J. Bunce, J. T. Clarke, S. W. H. Cowley, F. J. Crary, M. K. Dougherty, J.-C. Gérard, D. Grodent, K. C. Hansen, W. S. Kurth, D. G. Mitchell, W. R. Pryor, T. S. Stallard, D. L. Talboys, and S. Wannawichian (2009), Saturn's equinoctial auroras, *Geophysical Research Letters*, *36*, L24102, doi:10.1029/2009GL041491.

O'Donoghue, J., T. S. Stallard, H. Melin, G. H. Jones, S. W. H. Cowley, S. Miller, K. H. Baines, and J. S. D. Blake (2013), The domination of Saturn's low-latitude ionosphere by ring 'rain', *Nature*, *496*, 193–195, doi:10.1038/nature12049.

O'Donoghue, J., T. S. Stallard, H. Melin, S. W. H. Cowley, S. V. Badman, L. Moore, S. Miller, C. Tao, K. H. Baines, and J. S. D. Blake (2014), Conjugate observations of Saturn's northern and southern H3+ aurorae, *Icarus*, *229*, 214–220, doi:10.1016/j.icarus.2013.11.009.

Oka, T. (2006), Interstellar Chemistry Special Feature: Interstellar H_3^+, *Proceedings of the National Academy of Science*, *103*, 12,235–12,242, doi:10.1073/pnas.0601242103.

Provan, G., D. J. Andrews, C. S. Arridge, A. J. Coates, S. W. H. Cowley, S. E. Milan, M. K. Dougherty, and D. M. Wright (2009), Polarization and phase of planetary-period magnetic field oscillations on high-latitude field lines in Saturn's magnetosphere, *J. Geophys. Res. (Space Physics)*, *114*, A02225, doi:10.1029/2008JA013782.

Provan, G., D. J. Andrews, C. S. Arridge, A. J. Coates, S. W. H. Cowley, G. Cox, M. K. Dougherty, and C. M. Jackman (2012), Dual periodicities in planetary-period magnetic field oscillations in Saturn's tail, *J. Geophys. Res. (Space Physics)*, *117*, A01209, doi:10.1029/2011JA017104.

Provan, G., L. Lamy, S. W. H. Cowley, and M. K. Dougherty (2014), Planetary period oscillations in Saturns magnetosphere: Comparison of magnetic oscillations and SKR modulations in the post-equinox interval, *J. Geophys. Res. (Space Physics), submitted*, doi: 10.1002/2014JA020011.

Radioti, A., D. Grodent, J.-C. Gérard, S. E. Milan, B. Bonfond, J. Gustin, and W. Pryor (2011), Bifurcations of the main auroral ring at Saturn: ionospheric signatures of consecutive reconnection events at the magnetopause, *J. Geophys. Res.*, *116*, A11209, doi: 10.1029/2011JA016661.

Radioti, A., D. Grodent, J.-C. Gérard, B. Bonfond, J. Gustin, W. Pryor, J. M. Jasinski, and C. S. Arridge (2013), Auroral signatures of multiple magnetopause reconnection at Saturn, *Geophys. Res. Lett.*, *40*, 4498–4502, doi:10.1002/grl.50889.

Raynaud, E., E. Lellouch, J.-P. Maillard, G. R. Gladstone, J. H. Waite, B. Bézard, P. Drossart, and T. Fouchet (2004), Spectro-imaging observations of Jupiter's 2-μm auroral emission. I. H_3^+ distribution and temperature, *Icarus*, *171*, 133–152, doi:10.1016/j.icarus.2004.04.020.

Sandel, B. R., and A. L. Broadfoot (1981), Morphology of Saturn's aurora, *Nature*, *292*, 679–682, doi:10.1038/292679a0.

Sandel, B. R., D. E. Shemansky, A. L. Broadfoot, J. B. Holberg, G. R. Smith, J. C. McConnell, D. F. Strobel, S. K. Atreya, T. M. Donahue, H. W. Moos, D. M. Hunten, R. B. Pomphrey, and S. Linick (1982), Extreme ultraviolet observations from the Voyager 2 encounter with Saturn, *Science*, *215*, 548–553, doi:10.1126/science.215.4532.548.

Smith, C. G. A., A. D. Aylward, G. H. Millward, S. Miller, and L. E. Moore (2007), An unexpected cooling effect in Saturn's upper atmosphere, *Nature*, *445*, 399–401, doi: 10.1038/nature05518.

Southwood, D. (2011), Direct evidence of differences in magnetic rotation rate between Saturn's northern and southern polar regions, *J. Geophys. Res. (Space Physics)*, *116*, A01201, doi: 10.1029/2010JA016070.

Southwood, D. J., and S. W. H. Cowley (2014), The origin of Saturn's magnetic periodicities: Northern and southern current systems, *J. Geophys. Res. (Space Physics)*, *119*, 1563–1571, doi:10.1002/2013JA019632.

Stallard, T. S., H. Melin, S. Miller, J. O' Donoghue, S. W. H. Cowley, S. Badman, A. Adriani, R. H. Brown, and K. H. Baines (2012a), Temperature changes and energy inputs in giant planet atmospheres: what we are learning from H_3^+, *Phil. Trans. Roy. Soc.*, *370*, 5213–5224, doi:10.1098/rsta.2012.0028.

Stallard, T. S., H. Melin, S. Miller, S. V. Badman, R. H. Brown, and K. H. Baines (2012b), Peak emission altitude of Saturn's H_3^+ aurora, *Geophys. Res. Lett.*, *39*, L15103, doi: 10.1029/2012GL052806.

Yelle, R. V., and S. Miller (2004), *Jupiter's thermosphere and ionosphere*, pp. 185–218.